**ARTICLE** AIP Advances scitation.org/journal/adv

# Epitaxial growth of $\beta$ -Ga<sub>2</sub>O<sub>3</sub> by hot-wall MOCVD $\otimes$



Cite as: AIP Advances 12, 055022 (2022); doi: 10.1063/5.0087571

Submitted: 8 March 2022 • Accepted: 2 May 2022 •

Published Online: 18 May 2022







Daniela Gogova,<sup>1,2</sup> D Misagh Ghezellou,<sup>2</sup> Dat Q. Tran,<sup>1,2</sup> D Steffen Richter,<sup>1,3,4</sup> D Alexis Papamichail,<sup>1,2,4</sup> D Jawad ul Hassan,<sup>2</sup> D Axel R. Persson,<sup>1,2</sup> Per O. Å. Persson,<sup>2</sup> Olof Kordina,<sup>1,2</sup> Bo Monemar,<sup>1,2</sup> Matthew Hilfiker. Dathias Schubert. Matthew Hilfiker. Dathias Schubert. Matthew Hilfiker. Dathias Schubert. Dathias Plamen P. Paskov. Dathias Dathias Schubert. Dathias Dathias Schubert. Dathias Dathias Schubert. Dathias Da

## **AFFILIATIONS**

- <sup>1</sup> Center for III-Nitride Technology, C3NiT-Janzen, Linköping University, 581 83 Linköping, Sweden
- <sup>2</sup> Department of Physics, Chemistry and Biology, IFM, Linköping University, 581 83 Linköping, Sweden
- Solid State Physics and NanoLund, Lund University, P. O. Box 118, 221 00 Lund, Sweden
- <sup>4</sup>THz Materials Analysis Center (THeMAC), Linköping University, 581 83 Linköping, Sweden
- Department of Electrical and Computer Engineering, University of Nebraska-Lincoln, Lincoln, Nebraska 68588, USA

### **ABSTRACT**

The hot-wall metalorganic chemical vapor deposition (MOCVD) concept, previously shown to enable superior material quality and high performance devices based on wide bandgap semiconductors, such as Ga(Al)N and SiC, has been applied to the epitaxial growth of  $\beta$ -Ga<sub>2</sub>O<sub>3</sub>. Epitaxial  $\beta$ -Ga<sub>2</sub>O<sub>3</sub> layers at high growth rates (above 1  $\mu$ m/h), at low reagent flows, and at reduced growth temperatures (740 °C) are demonstrated. A high crystalline quality epitaxial material on a c-plane sapphire substrate is attained as corroborated by a combination of x-ray diffraction, high-resolution scanning transmission electron microscopy, and spectroscopic ellipsometry measurements. The hot-wall MOCVD process is transferred to homoepitaxy, and single-crystalline homoepitaxial  $\beta$ -Ga<sub>2</sub>O<sub>3</sub> layers are demonstrated with a  $\bar{2}01$ rocking curve width of 118 arc sec, which is comparable to those of the edge-defined film-fed grown ( $\bar{2}01$ )  $\beta$ -Ga<sub>2</sub>O<sub>3</sub> substrates, indicative of similar dislocation densities for epilayers and substrates. Hence, hot-wall MOCVD is proposed as a prospective growth method to be further explored for the fabrication of  $\beta$ -Ga<sub>2</sub>O<sub>3</sub>.

© 2022 Author(s). All article content, except where otherwise noted, is licensed under a Creative Commons Attribution (CC BY) license (http://creativecommons.org/licenses/by/4.0/). https://doi.org/10.1063/5.0087571

Gallium oxide has gained substantial research interest recently due to its ultra-wide bandgap energy of ~5 eV<sup>1,2</sup> and the availability of affordable native substrates grown by inexpensive melt growth approaches.<sup>3</sup> The thermodynamically stable polymorph of gallium oxide, monoclinic  $\beta$ -Ga<sub>2</sub>O<sub>3</sub>, has a breakdown electric field in the range of 6-8 MV/cm, which is three times larger than the respective values of GaN and SiC, resulting in four to ten times higher Baliga's figure of merit for  $\beta$ -Ga<sub>2</sub>O<sub>3</sub>, respectively.<sup>3,4</sup> Consequently, β-Ga<sub>2</sub>O<sub>3</sub> holds a strong potential for next generation high power electronics,5 which is the key to enable considerable energy savings in conversion and transport of electricity for green economy and sustainable development. Significant research efforts have been directed toward the development of different growth techniques for  $\beta$ -Ga<sub>2</sub>O<sub>3</sub> heteroepitaxy and homoepitaxy, including molecular beam epitaxy (MBE), 6-9 plasma-enhanced atomic layer deposition (ALD), f<sub>0,11</sub> pulsed laser deposition (PLD), f<sub>12-14</sub> mist chemical vapor deposition (mist-CVD), f<sub>15</sub> plasma CVD, f<sub>16-18</sub> halide vapor phase epitaxy (HVPE),<sup>19</sup> and metalorganic CVD (MOCVD) employing cold-wall reactors.<sup>20</sup>

When c-plane sapphire is employed as a substrate in heteroepitaxy,  $\beta$ -Ga<sub>2</sub>O<sub>3</sub> grows with the ( $\bar{2}01$ ) orientation parallel to the sapphire (0001) plane. <sup>26–28</sup> Six  $\beta$ -Ga<sub>2</sub>O<sub>3</sub> (201) rotational domains with equal volume fractions form on on-axis c-plane sapphire.<sup>27</sup> For *c*-plane sapphire off-cut toward the *a*-plane, the number of rotational domains decreased from six to three separated by 120° and one of the domains became predominant with the increasing offangle. In contrast, for off-cut toward the m-plane, the six domains remained but showed different volume fractions, as deduced from pole scan XRD intensities.<sup>27</sup> Almost complete suppression of all but one  $\beta$ -Ga<sub>2</sub>O<sub>3</sub> (201) domain orientation was reported recently.<sup>29</sup> The microstructural comparison of  $\beta$ -Ga<sub>2</sub>O<sub>3</sub> grown on c-plane sapphire by MBE, PLD, and MOCVD revealed the presence of a threemonolayer-thick pseudomorphically grown layer of rhombohedral α-Ga<sub>2</sub>O<sub>3</sub> at the interface with the substrate, independent of the

a) Author to whom correspondence should be addressed: vanya.darakchieva@liu.se and vanya.darakchieva@ftf.lth.se

growth method.<sup>30</sup> On top of the  $\alpha$ -Ga<sub>2</sub>O<sub>3</sub> layer, plastically relaxed  $\beta$ -Ga<sub>2</sub>O<sub>3</sub> grew with the six rotational domains.<sup>30</sup> Recently, extensive research was devoted to the homoepitaxial growth of  $\beta$ -Ga<sub>2</sub>O<sub>3</sub> on bulk native substrates for efficient power switching devices. Homoepitaxial  $\beta$ -Ga<sub>2</sub>O<sub>3</sub> layers with controlled doping and with different surface crystallographic orientations, e.g., (100), (010), (001), and ( $\overline{2}$ 01), have been demonstrated.<sup>22,23,25,31-37</sup>

Achieving the growth of high-quality layers and device heterostructures with controlled doping presents one of the most significant challenges for future adoption of  $\beta\text{-}\text{Ga}_2\text{O}_3$  in electronics. MOCVD is the method of choice in contemporary semiconductor technology to obtain device quality epitaxial structures, and it is scalable with high throughput. Hot-wall MOCVD is a unique modification demonstrated recently with success for state-of-the-art wide bandgap SiC $^{38,39}$  and group-III nitride materials  $^{40-42}$  for applications in high-power high-frequency electronics  $^{43,44}$  and quantum technology. The hot-wall MOCVD enables industry-relevant growth rates and delivers superior material purity and structural quality.  $^{46,47}$ 

In this work, we explore hot-wall MOCVD for the growth of  $\beta$ -Ga<sub>2</sub>O<sub>3</sub> using an injector with isolated injection of precursors. Aiming for a cost-effective process, we target establishing a growth window at relatively low temperatures below 800 °C combined with a high growth rate and low reagent consumption. The interplay between growth regimes and structural properties of  $\beta$ -Ga<sub>2</sub>O<sub>3</sub> layers on c-plane sapphire is discussed, and a heteroepitaxial material of good crystal and optical quality at a growth temperature of 740 °C and a high growth rate  $\geq 1~\mu$ m/h is demonstrated. The process is also successfully transferred to homoepitaxy on ( $\bar{2}$ 01)-oriented  $\beta$ -Ga<sub>2</sub>O<sub>3</sub> substrates. Thus, we have demonstrated the application potential of the hot-wall MOCVD approach for the epitaxial growth of gallium oxide.

An upgraded custom-built low-pressure horizontal hot-wall MOCVD reactor (Epiluvac AB) was used for  $\beta\text{-}\mathrm{Ga}_2\mathrm{O}_3$  growth based on earlier designs successfully implemented for the growth of SiC.  $^{38}$  A CAD drawing of the water cooled injector and the susceptor in the hot-wall MOCVD reactor with an adjustable distance between the injector and susceptor is presented in Fig. 1. The SiC-coated graphite susceptor was heated by a radio frequency inductive coil and allowed deposition temperatures in a large range from 400 to  $1200\,^{\circ}\mathrm{C}$ . Isolated injections of the gallium and oxygen precursors to avoid preliminary gas phase reactions and a gas foil rotation

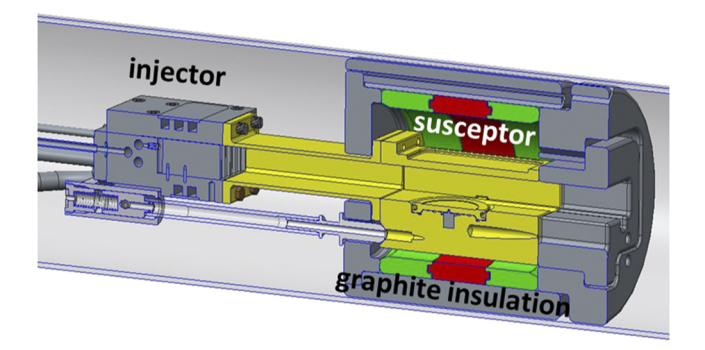


**FIG. 1.** A CAD drawing of the water cooled injector with isolated injection of precursors and the susceptor in the hot-wall MOCVD reactor.

for uniform deposition on up to 2 in. wafers were incorporated. Trimethylgallium (TMGa) was selected as a precursor of Ga in our study because it is more cost-effective compared to the commonly employed triethylgallium due to its higher vapor pressure and faster reaction kinetics, enabling generally higher growth rates, and lower cost. The TMGa bubbler temperature was kept at 5 °C in all series of experiments. Highly pure oxygen gas (O2) and argon (Ar) were employed as a source of oxygen and a carrier gas, respectively. In order to establish the MOCVD growth windows, the depositions were performed on readily available and relatively inexpensive sapphire substrates with an on-axis c-plane orientation and with 5° off-cut toward the a-plane. For transferring of the process developed to homoepitaxy, edge-defined film-fed grown β-Ga<sub>2</sub>O<sub>3</sub> substrates (Novel Crystal Technology, Inc.) with the (201) orientation were selected for comparative reasons. Before each growth experiment, the substrates were ultrasonically cleaned with acetone, ethanol, and deionized water for 5 min each, dried in pure N2, and then loaded into the reactor chamber.

Initial multi-parameter growth optimization was performed as a function of growth temperature and pressure and of reagent flows and ratios in order to attain epitaxial  $\beta$ -Ga<sub>2</sub>O<sub>3</sub> layers on on-axis c-plane sapphire substrates at temperatures below 800 °C (from 650 to 780 °C). Based on the evaluation of experimental results, a growth temperature of 720 °C was selected as the optimal one for further optimizing the growth rate. For this purpose, a set of samples at different growth pressures from 50 mbar to 200 mbar was grown using a TMGa molar flow rate of 106 mol/min, an oxygen flow rate of 515 ml/min, and an O2/TMGa ratio of 200. This set of samples is hereafter referred to as the high-pressure growth window. The VI/III ratio of 200 is relatively low compared to the values typically reported in the literature for the MOCVD growth of  $\beta$ -Ga<sub>2</sub>O<sub>3</sub>. However, the gas phase and surface reactions, blocking incorporation sites, etc., are expected to be different in the case of the hot-wall reactor design.<sup>48</sup> The inherent to hot-wall MOCVD highly uniform temperature distribution vertically and laterally in the growth zone also facilitates high cracking efficiency of the precursors, preventing growth-limited species consumption by gas-phase adduct formation and, hence, a high efficiency of the chemical reactions. The O/Ga ratio further affects the formation energy of C substitutional defects, 49 which may interfere with the electron conductivity.<sup>50</sup> More recently, C-H complexes were suggested to play a role for the compensation in  $\beta$ -Ga<sub>2</sub>O<sub>3</sub> grown by MOCVD.<sup>51</sup> In this respect, it is worth mentioning that hot-wall MOCVD was shown to enable non-passivated Mg acceptors by H in as-grown GaN:Mg.52 The effect of C incorporation on the electric conductivity in hotwall MOCVD grown β-Ga<sub>2</sub>O<sub>3</sub> layers will be explored in future works.

In order to improve the cost-effectiveness of the process, a second set of  $\beta\text{-}\mathrm{Ga_2O_3}$  layers was grown with reduced reagent and carrier gas flows to one third while maintaining approximately the same VI/III ratio and a similar growth temperature of 740 °C. In this case, the deposition pressure was varied within the range of 10–50 mbar. This set of samples is hereafter referred to as the low–pressure growth window. In addition, homoepitaxial growth was performed at 50 mbar using the low–pressure growth window reagent conditions. Before the growth was initiated, the  $\beta\text{-}\mathrm{Ga_2O_3}$  substrate was annealed at 740 °C in situ in an Ar atmosphere for 1 h.

The crystal quality of the epitaxial layers was analyzed by x-ray diffraction (XRD).  $2\theta/\theta$  scans were measured in a Bragg-Brentano configuration using an x-ray powder diffractometer X'celerator (Panalytical). Rocking curves ( $\omega$ -scans, RC), reciprocal space maps (RSM), and pole figure measurements were performed with a highresolution XRD (HRXRD) diffractometer Empyrean (Panalytical) using a 2-bounce Ge(220) monochromator as incident-beam optics. A 3-bounce Ge(220) detector and a parallel plate collimator were used on the detector side in the  $\omega$ -scans and in the pole figure measurements, respectively. Scanning transmission electron microscopy (STEM) was performed using the double corrected Linköping FEI Titan 60-300 STEM, operated in scanning transmission electron microscopy mode and at 300 kV, employing a high-angle annular dark-field (HAADF) detector with collection angles between 84 and 200 mrad. Scans were either acquired as single scans or reconstructed from multiple scans.<sup>53</sup>

Generalized spectroscopic ellipsometry (GSE) using a dual-rotating compensator ellipsometer (RC2, J.A. Woollam Co., Inc.) was performed in the range from 0.75 to 6.5 eV for the characterization of sample optical properties. Mueller matrix element spectra were measured at angles of incidence of  $\Phi_a = 35^{\circ}$ ,  $45^{\circ}$ ,  $55^{\circ}$ , and  $65^{\circ}$  and at multiple azimuth sample rotations in steps of  $45^{\circ}$ . The experimental data are analyzed using a critical-point model lineshape function approach, permitting the determination of direct band-to-band transitions, exciton energies, amplitude, broadening, and transition dipole orientations. The bandgap energy can be directly compared with other results to be reported in the future. For the epitaxial layers discussed in this work, due to the

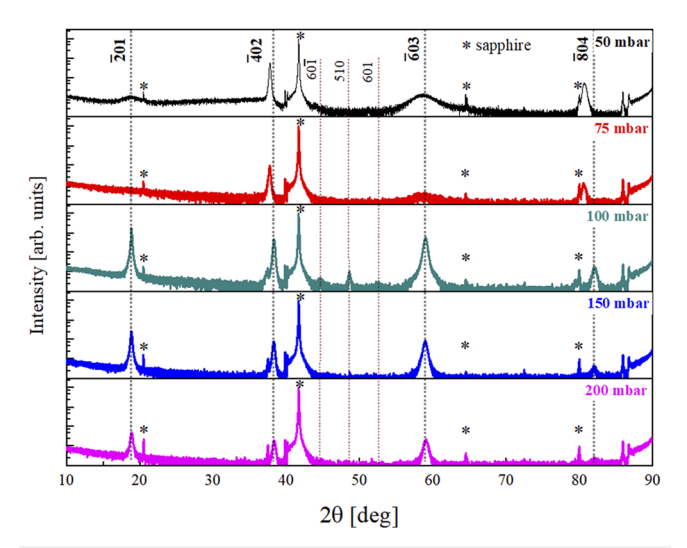
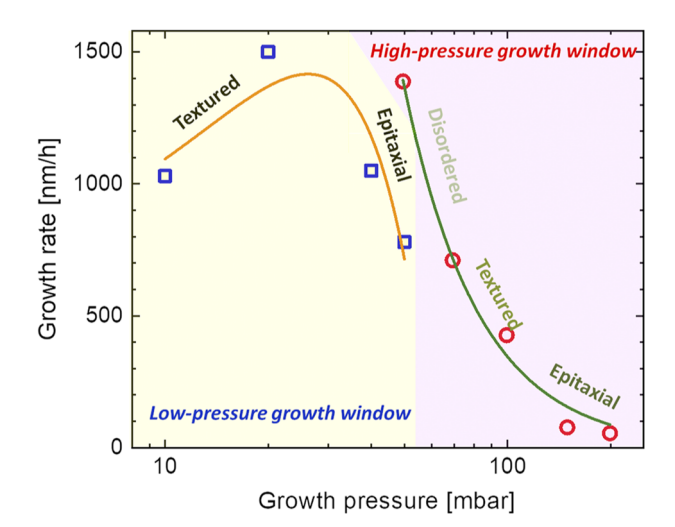


**FIG. 2.**  $2\theta/\theta$  scans in Bragg–Brentano geometry for the  $\beta$ -Ga<sub>2</sub>O<sub>3</sub> layers from the high-pressure growth window grown on the on-axis c-plane sapphire and at various pressures. The values of the growth pressures are indicated above the respective spectra. The  $\beta$ -Ga<sub>2</sub>O<sub>3</sub>  $\bar{2}01$ ,  $\bar{4}02$ ,  $\bar{6}03$ , and  $\bar{8}04$  Bragg reflections at 18.9°, 37.8°, 58.7°, and 80.7°, respectively.<sup>54</sup> are indicated with black dotted lines. Some additional  $\beta$ -Ga<sub>2</sub>O<sub>3</sub> peaks,  $\bar{6}01$ , 510 and  $\bar{6}01$ , appearing in the spectrum of the layer grown at 100 mbar are indicated with red thin dotted lines. The 0003, 0006, and 0009 Bragg reflections of the c-plane sapphire at 2 $\theta$  values of 21.00°, 41.69°, and 64.5° and the substrate artifact at ~80° (Ref. 54) are indicated by asterisks.

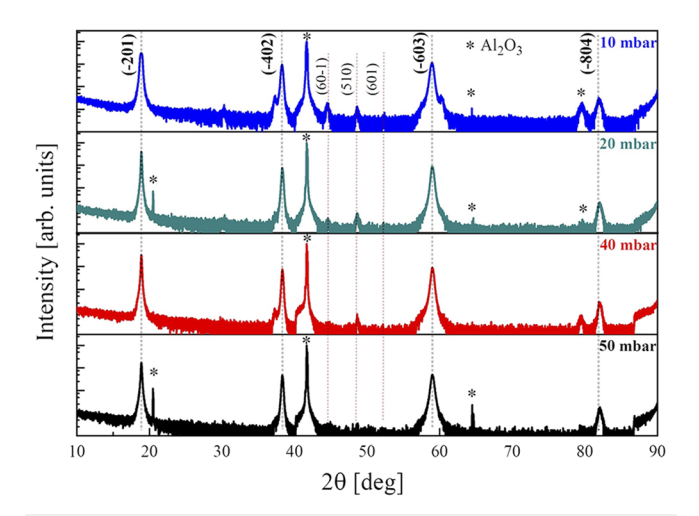
specific domain structure and crystallographic orientation, an effective medium model is developed. Thereby, we calculate a weight average of a dielectric function model tensor accounting for the contributions of different rotational domains to the overall optical polarizability.

Figure 2 illustrates the  $2\theta/\theta$  scans of the set of samples from the high-pressure window grown at varying deposition pressures from 50 to 200 mbar. The  $\beta$ -Ga<sub>2</sub>O<sub>3</sub> diffraction peaks are indexed, and the sapphire diffraction peaks are indicated by asterisks. The experimental results reveal that at a relatively high growth pressure above 100 mbar, epitaxial  $\beta$ -Ga<sub>2</sub>O<sub>3</sub> layers with a single (201)-orientation are grown with their (201) plane parallel to the sapphire (0001) plane. As it can be seen from Fig. 2, only the 201, 402, 603, and 804 Bragg peaks of the monoclinic gallium oxide phase can be detected for layers grown at 150 and 200 mbar. At 100 mbar, some crystallites with an orientation different from the main ( $\bar{2}01$ ) orientation, i.e.,  $\beta$ -Ga<sub>2</sub>O<sub>3</sub> ( $60\bar{1}$ ), (510) and (601) crystallographic orientations, are observed in the XRD spectra. Note that the XRD peak intensity associated with these additional crystallites is much smaller compared to the intensity of the main 201-peak family; however, their incorporation is not desirable in terms of β-Ga<sub>2</sub>O<sub>3</sub> integration in device hetero-structures. At a growth pressure below 100 mbar, the β-Ga<sub>2</sub>O<sub>3</sub> peaks broaden significantly and decrease in intensity, indicating a significant degree of disorder.

The growth rate as a function of the deposition pressure for the *high-pressure growth window* samples is illustrated in Fig. 3. At growth pressures below 100 mbar, the large amount of reagents and carrier gasses might lead to very fast reactions, resulting in the observed high growth rates up to  $1.4 \,\mu\text{m/h}$ . Although a high growth rate is desirable in terms of process efficiency, in these instances, the layers are no longer epitaxial but textured and become highly disordered as the pressure further decreases (see Fig. 2).



**FIG. 3.** Growth rate as a function of deposition pressure for the two sample sets. The red circles indicate the results for the layers from the high-pressure growth window, while those for the layers from the low-pressure growth window are shown as blue squares. The curves are guides to the eye.



**FIG. 4.** Same as in Fig. 2 but for the samples from the low-pressure growth window.

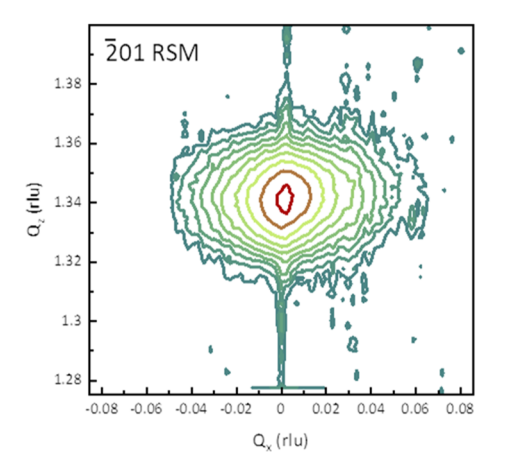
At very high growth rates and relatively high pressures, a deviation from the thermodynamic equilibrium occurs and the Ga and O adatoms have insufficient time to migrate and arrange in a crystal lattice. Therefore, they form clusters with the other adatoms. In addition, the atoms in the layer are not densely stacked as it is in a typical CVD process and a highly disordered phase is formed. The growth rate decreases rapidly with increasing pressure, which can be attributed to a hampered atom diffusion as a result of the increased thickness of the boundary layer. In addition, at higher pressures, there is enhancement of gas phase reactions, which contributes to further reduction of the growth rate. For the single-orientation epitaxial layers, grown at pressures above 100 mbar (Fig. 2), the growth rate is only of the order of 100 nm/h (Fig. 3), which is too low for practical applications.

Therefore, as a next step, we aimed at establishing a smaller growth window for the deposition of epitaxial  $\beta$ -Ga<sub>2</sub>O<sub>3</sub> with a single (201)-orientation and a high growth rate, minimizing reactive and carrier gas flows. To reach this goal, the total gas flow

and growth pressures were considerably decreased in comparison to the values in the high-pressure growth window. More specifically, the total gas flow was reduced to one third with a TMGa molar flow rate of 45 mol/min and an oxygen flow rate of 200 ml/min while maintaining approximately the same VI/III ratio and a similar growth temperature of 740 °C. The deposition pressure was varied within the range of 10-50 mbar. Figure 4 presents the respective  $2\theta/\theta$  scans, and the growth rates for the series are compared to the results for layers from the *high* – *pressure growth window* in Fig. 3. Epitaxial layers with single (201) crystallographic orientations were achieved at growth pressures of 50 and 40 mbar. At 20 mbar, the β-Ga<sub>2</sub>O<sub>3</sub> 510 Bragg peak with a very low intensity appears, while for the layer grown at 10 mbar, an additional 601 Bragg peak could also be detected. Decreasing the reagent flow rates and deposition pressure with other CVD growth parameters kept constant leads to a decrease in Ga supersaturation, which is essential for high crystalline quality growth. The small total flow of reactive and carrier gases in the low-pressure growth window allows laminar flows in the reactor and growth close to thermodynamic equilibrium and hence improved crystalline quality. The RSM and RC single scans of the 201 on-axis peak as illustrated in Fig. 5 indicate good crystalline quality of the heteroepitaxial material. The full width at half maximum of the RC has been determined as 1.5°, which is very well comparable to the reported literature values for the best MOCVD-grown layers.<sup>55</sup> In the radial direction, the RSM is fully symmetric, suggesting a high coherence length of the crystalline domains with no indication of heterogeneous

At the same time, high growth rates of up to 1.5  $\mu$ m/h compatible with industry relevant values are reached. These results demonstrate the high application potential of the hot-wall MOCVD  $\beta$ -Ga<sub>2</sub>O<sub>3</sub> growth process for industry utilization.

XRD pole figures of the  $\beta$ -Ga<sub>2</sub>O<sub>3</sub> epilayers grown with the low-pressure growth window conditions simultaneously on on-axis and off-cut sapphire reveal that for on-axis substrates, six  $\beta$ -Ga<sub>2</sub>O<sub>3</sub> ( $\overline{2}$ 01) rotational domains, rotated by 60°, are observed with equal distributions (Fig. S1 in the supplementary material), while for the case of the off-cut substrates, one set of three domains, rotated by 120°, is predominant and the other three nearly disappear (Fig. S2 in the supplementary material). These results are



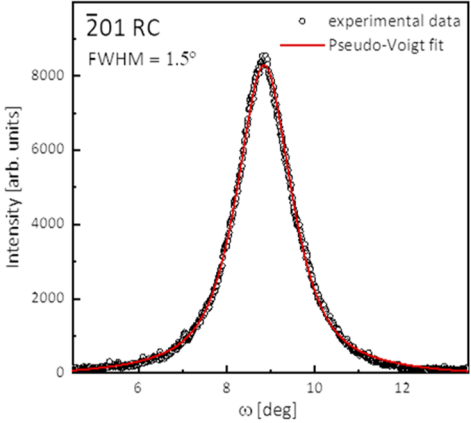


**FIG. 5.** (Left) RSM around the β-Ga<sub>2</sub>O<sub>3</sub>  $\overline{2}01$  reciprocal point and (right)  $\overline{2}01$  RC for the layer from the low – pressure growth window grown on c-plane sapphire at 50 mbar.

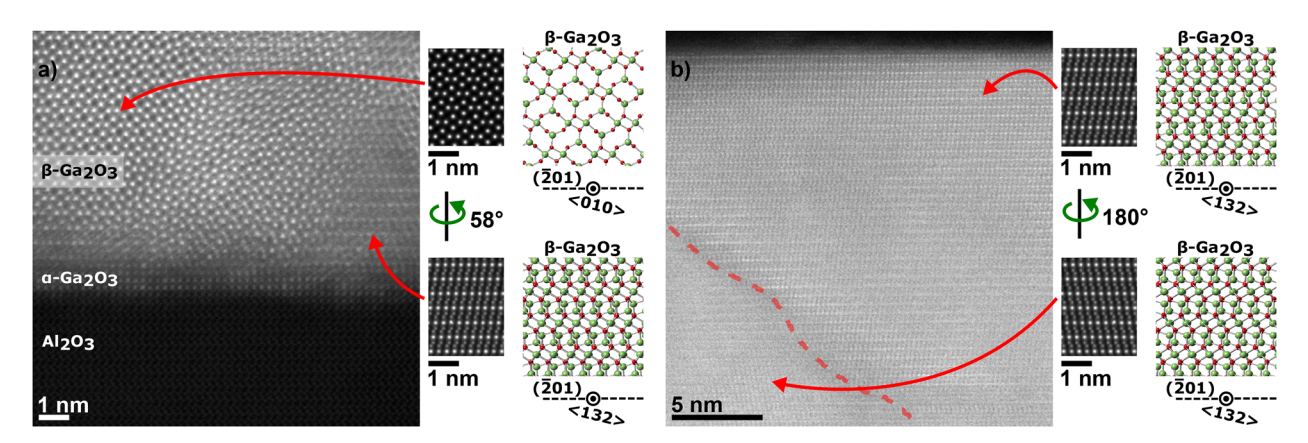


FIG. 6. STEM images and image simulations of a  $\beta$ -Ga<sub>2</sub>O<sub>3</sub> heteroepitaxial layer from regions close to the sapphire substrate ( $\alpha$ -AL<sub>2</sub>O<sub>3</sub>) (a) and close to the top surface (b). The model for  $\beta$ -Ga<sub>2</sub>O<sub>3</sub> is shown next to the images with their respective projection direction and the horizontal ( $\bar{2}$ 01) plane indicated. Green atoms indicate Ga, and red ones indicate O. The projections of the model are simulated and matched to regions within the images. In (a), both (010) and (132) projections are observed, while in (b), two larger grains are observed with projections in (132) directions, 180° rotated relative to each other. This matches the six-fold rotational ( $\bar{2}$ 01) domains, observed by XRD (Fig. S1 in the supplementary material).

consistent with previous reports.<sup>26</sup> The use of the off-cut substrates leads to slightly narrower rocking curves, indicating some amelioration of overall crystalline quality and decreased defect density. In addition, the off-cut substrates were found to be beneficial for suppressing the additional crystallographic orientations at low growth pressures.

The domain structure is further confirmed by high-resolution STEM, revealing details at the atomic scale. Figure 6(a) shows a cross-sectional HAADF-STEM image of the epilayer grown at 50 mbar under low-pressure growth window conditions in the vicinity of the interface with the on-axis sapphire substrate. The first few atomic layers exhibit an orthorhombic α-Ga<sub>2</sub>O<sub>3</sub> crystal structure with [0001] along the growth direction, seen as a similar pattern as for the α-Al<sub>2</sub>O<sub>3</sub> substrate but with higher intensity (HAADF-STEM exhibits Z-contrast), which is in agreement with earlier observations.<sup>30</sup> After the first few atomic layers, the growth transitions to ( $\bar{2}01$ )-oriented  $\beta$ -Ga<sub>2</sub>O<sub>3</sub>. Multiple grains with varying azimuth rotations are observed in the STEM images in Fig. 6. The low-index projection direction of (010) and (132) is distinguishable, which is rotated  $\sim 58^{\circ}$  relative to the first one [Fig. 6(a)]. Further away from the interface with the substrate, larger grains develop [Fig. 6(b)] with clear mirroring, indicative of the six-fold

The high structural quality of the heteroepitaxial layers is also manifested in similar excitonic and band-to-band transition parameters of  $\beta$ -Ga<sub>2</sub>O<sub>3</sub>, as determined from spectroscopic ellipsometry analysis. The different contributions of the six rotational ( $\bar{2}01$ )-oriented domains to the tensor of the dielectric function are averaged as an additive effective medium. The rotational domains render the optical response effectively uniaxial as a cylindrical symmetry with respect to the optic axis of the c-plane sapphire substrate is established. This is even the case for layers grown on off-axis substrates with three dominant rotational domains (Fig. S2 in the supplementary material). No optical difference between samples on on-axis and off-cut substrates is observed. Figure 7 shows

exemplary measured and modeled ellipsometry data for a  $\beta$ -Ga<sub>2</sub>O<sub>3</sub> layer grown with the *low-pressure growth window* conditions at 50 mbar on on-axis sapphire. For comparison, model-generated data using the parameters of bulk  $\beta$ -Ga<sub>2</sub>O<sub>3</sub> from Ref. 2 are also shown. High material quality of our epitaxial  $\beta$ -Ga<sub>2</sub>O<sub>3</sub> is inferred not only from the transparency below the bandgap that causes layer interferences but also by no increased broadening of the absorption edge

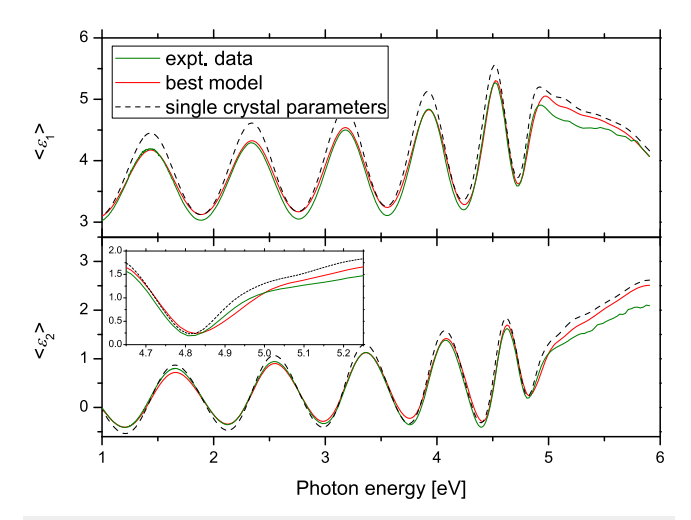


**FIG. 7.** Measured and modeled spectroscopic ellipsometry data in terms of the pseudo-dielectric function  $\langle \varepsilon \rangle = \langle \varepsilon_1 \rangle + i \langle \varepsilon_2 \rangle$  at an angle of incidence of  $65^\circ$  for a  $\beta$ -Ga $_2$ O $_3$  layer from the low-pressure growth window grown on a c-plane sapphire substrate at 50 mbar. The six equally distributed rotational domains render the film optically uniaxial and the response pseudo-isotropic. The layer interference oscillations below 5 eV demonstrate the transparency of the film. The inset shows an enlarged view at  $\langle \varepsilon_2 \rangle$  at the bandgap. The dashed line represents model-generated data using parameters reported in Ref. 2. Multiple angles of incidence were included in the modeling.

as compared to single crystalline bulk  $\beta$ -Ga<sub>2</sub>O<sub>3</sub>. Modeling is mostly sensitive to the energetically lowest band-to-band transition, which is polarized in the monoclinic plane. The excitonic binding energy of 120 meV is assumed to be unchanged. We find a slight redshift of the related critical point at 5.04 eV of ~10 meV, which may be attributed to a small level of residual strain. For Furthermore, as can be seen in Fig. 7, the transition amplitudes are about 10% lower than those found for bulk single crystals. The lowered amplitudes can be related to the presence of grain boundaries due to the rotational domain structure of the epilayers (see Fig. 6), which affects particularly Wannier–Mott excitons and, hence, decreases the excitonic absorption enhancement. The higher-energy transitions could not be reliably assessed due to the rotational domain structure

Finally, we have performed homoepitaxial growth under the low–pressure growth window conditions at a pressure of 50 mbar. The  $2\theta/\theta$  scan of the homoepitaxial layer on the  $(\bar{2}01)$   $\beta$ -Ga<sub>2</sub>O<sub>3</sub> substrate (Fig. S4 in the supplementary material) shows only the  $\bar{2}01$  Bragg peak family. The  $\bar{2}01$  rocking curve full width at half maximum of the homoepitaxial layer is 118 arc sec, which is comparable to that of the bulk edge-defined film-fed grown  $\beta$ -Ga<sub>2</sub>O<sub>3</sub> substrate (88.8 arc sec) (see Fig. S5 in the supplementary material). This indicates similar dislocation densities for epitaxial layers and substrates.

In summary, we have presented a new hot-wall approach to the MOCVD growth of epitaxial  $\beta\textsc{-}\text{Ga}_2\textsc{O}_3$  layers at reduced temperatures and reagent flows and at high growth rates using a TMGa precursor. The heteroepitaxial material on basal plane sapphire with state-of-the-art quality and homoepitaxial  $\beta\textsc{-}\text{Ga}_2\textsc{O}_3$  layers on (201) native substrates with crystalline quality approaching that of the melt grown substrates have been demonstrated. The newly developed hot-wall MOCVD gallium oxide reactor concept offers a versatile method with the potential for cost-effective industrially viable epitaxial growth.

See the supplementary material for the details about XRD characterization of hetero- and homoepitaxial layers and GSE measured and modeled spectra of the samples grown simultaneously under the *low-pressure growth window* conditions at 50 mbar on on-axis and off-cut *c*-plane sapphire.

This work was supported by the Swedish Energy Agency under Award No. P45396-1 and performed within the framework of the Competence Center for III-Nitride Technology, C3NiT-Janzén supported by the Swedish Governmental Agency for Innovation Systems (VINNOVA) under the Competence Center Program Grant No. 2016-05190, Linköping University, Chalmers University of Technology, Ericsson, Epiluvac, FMV, Gotmic, Hexagem, Hitachi Energy, On Semiconductor, Saab, SweGaN, and UMS. We further acknowledge support from the Swedish Research Council VR under Grant Nos. 2016-00889 and 2017-03714, the Swedish Foundation for Strategic Research under Grant Nos. RIF14-055, RIF14-074, and EM16-0024, and the Swedish Government Strategic Research Area in Materials Science on Functional Materials at Linköping University, Faculty Grant No. SFO Mat LiU No. 2009-00971. This work was supported, in part, by

the National Science Foundation (NSF) under Award Nos. NSF DMR 1808715 and NSF/EPSCoR RII Track-1: Emergent Quantum Materials and Technologies (EQUATE) under Award No. OIA-2044049 and by the Air Force Office of Scientific Research under Award Nos. FA9550-18-1-0360, FA9550-19-S-0003, and FA9550-21-1-0259. The KAW Foundation is also acknowledged for the support provided to the Linköping Electron Microscopy Laboratory.

### **AUTHOR DECLARATIONS**

### **Conflict of Interest**

The authors have no conflicts to disclose.

#### DATA AVAILABILITY

The data that support the findings of this study are available within the article and its supplementary material.

### **REFERENCES**

- <sup>1</sup>C. Sturm, J. Furthmüller, F. Bechstedt, R. Schmidt-Grund, and M. Grundmann, APL Mater. 3, 106106 (2015).
- <sup>2</sup>A. Mock, R. Korlacki, C. Briley, V. Darakchieva, B. Monemar, Y. Kumagai, K. Goto, M. Higashiwaki, and M. Schubert, Phys. Rev. B **96**, 245205 (2017).
- <sup>3</sup>M. Higashiwaki and G. H. Jessen, Appl. Phys. Lett. 112, 060401 (2018).
- <sup>4</sup>S. J. Pearton, J. Yang, P. H. Cary, F. Ren, J. Kim, M. J. Tadjer, and M. A. Mastro, Appl. Phys. Rev. 5, 011301 (2018).
- <sup>5</sup> J. Y. Tsao, S. Chowdhury, M. A. Hollis, D. Jena, N. M. Johnson, K. A. Jones, R. J. Kaplar, S. Rajan, C. G. Van de Walle, E. Bellotti, C. L. Chua, R. Collazo, M. E. Coltrin, J. A. Cooper, K. R. Evans, S. Graham, T. A. Grotjohn, E. R. Heller, M. Higashiwaki, M. S. Islam, P. W. Juodawlkis, M. A. Khan, A. D. Koehler, J. H. Leach, U. K. Mishra, R. J. Nemanich, R. C. N. Pilawa-Podgurski, J. B. Shealy, Z. Sitar, M. J. Tadjer, A. F. Witulski, M. Wraback, and J. A. Simmons, Adv. Electron. Mater. 4, 1600501 (2018).
- <sup>6</sup>M. Holland, C. R. Stanley, W. Reid, R. J. W. Hill, D. A. J. Moran, I. Thayne, G. W. Paterson, and A. R. Long, J. Vac. Sci. Technol., B 25, 1706 (2007).
- <sup>7</sup>M.-Y. Tsai, O. Bierwagen, M. E. White, and J. S. Speck, J. Vac. Sci. Technol., A **28**, 354 (2010).
- <sup>8</sup>H. Okumura, M. Kita, K. Sasaki, A. Kuramata, M. Higashiwaki, and J. S. Speck, Appl. Phys. Express 7, 095501 (2014).
- A. Mauze and J. Speck, in *Gallium Oxide: Materials Properties, Crystal Growth, and Devices*, edited by M. Higashiwaki and S. Fujita (Springer, Cham, 2020), p. 79.
  R. K. Ramachandran, J. Dendooven, J. Botterman, S. Pulinthanathu Sree, D. Poelman, J. A. Martens, H. Poelman, and C. Detavernier, J. Mater. Chem. A 2, 19232 (2014).
- <sup>11</sup> V. Wheeler, N. Nepal, L. Nyakiti, D. Boris, S. Walton, D. Meyer, and C. R. Eddy, Jr., in 2nd Workshop on Gallium Oxide and Related Materials, 2017.
- M. Orita, H. Ohta, M. Hirano, and H. Hosono, Appl. Phys. Lett. 77, 4166 (2000).
  M. Orita, H. Hiramatsu, H. Ohta, M. Hirano, and H. Hosono, Thin Solid Films 411, 134 (2002).
- <sup>14</sup>S. Müller, H. von Wenckstern, D. Splith, F. Schmidt, and M. Grundmann, Phys. Status Solidi A 211, 34 (2014).
- <sup>15</sup>S.-D. Lee, K. Kaneko, and S. Fujita, Jpn. J. Appl. Phys. 55, 1202B8 (2016).
- <sup>16</sup>L. Mochalov, A. Logunov, D. Gogova, S. Zelentsov, I. Prokhorov, N. Starostin, A. Letnianchik, and V. Vorotyntsev, Opt. Quantum Electron. 52, 510 (2020).
- <sup>17</sup>A. Logunov, L. Mochalov, D. Gogova, and V. Vorotyntsev, in 21st International Conference on Transparent Optical Networks (ICTON) (IEEE, 2019), p. Fr.P.27.

- <sup>18</sup>L. Mochalov, A. Logunov, T. Sazanova, D. Gogova, S. Zelentsov, P. Yunin, I. Prokhorov, V. Malyshev, and V. Vorotyntsev, in 22nd International Conference on Transparent Optical Networks (ICTON) (IEEE, 2020), p. W.P.27.
- <sup>19</sup> A. Almaev, V. Nikolaev, P. Butenko, S. Stepanov, A. Pechnikov, N. Yakovlev, I. Sinyugin, S. Shapenkov, and M. Scheglov, Phys. Status Solidi B 359, 2100306 (2022).
- <sup>20</sup>H. W. Kim and N. H. Kim, Mater. Sci. Eng.: B **110**, 34 (2004).
- <sup>21</sup> V. Gottschalch, K. Mergenthaler, G. Wagner, J. Bauer, H. Paetzelt, C. Sturm, and U. Teschner, Phys. Status Solidi A 206, 243 (2009).
- <sup>22</sup>D. Gogova, G. Wagner, M. Baldini, M. Schmidbauer, K. Irmscher, R. Schewski, Z. Galazka, M. Albrecht, and R. Fornari, J. Cryst. Growth 401, 665 (2014).
- <sup>23</sup>D. Gogova, M. Schmidbauer, and A. Kwasniewski, CrystEngComm 17, 6744 (2015)
- <sup>24</sup>M. Baldini, D. Gogova, K. Irmscher, M. Schmidbauer, G. Wagner, and R. Fornari, Cryst. Res. Technol. **49**, 552 (2014).
- <sup>25</sup> M. J. Tadjer, F. Alema, A. Osinsky, M. A. Mastro, N. Nepal, J. M. Woodward, R. L. Myers-Ward, E. R. Glaser, J. A. Freitas, A. G. Jacobs, J. C. Gallagher, A. L. Mock, D. J. Pennachio, J. Hajzus, M. Ebrish, T. J. Anderson, K. D. Hobart, J. K. Hite, and C. R. Eddy, Jr., J. Phys. D: Appl. Phys. 54, 034005 (2021).
- <sup>26</sup>S. Nakagomi and Y. Kokubun, J. Cryst. Growth **349**, 12 (2012).
- <sup>27</sup>Y. Oshima, E. G. Villora, and K. Shimamura, J. Cryst. Growth **410**, 53 (2015).
- <sup>28</sup>Y. Chen, H. Liang, X. Xia, P. Tao, R. Shen, Y. Liu, Y. Feng, Y. Zheng, X. Li, and G. Du, J. Mater. Sci.: Mater. Electron. 26, 3231 (2015).
- <sup>29</sup> S. Rafique, L. Han, A. T. Neal, S. Mou, J. Boeckl, and H. Zhao, Phys. Status Solidi A 215, 1700467 (2018).
- <sup>30</sup>R. Schewski, G. Wagner, M. Baldini, D. Gogova, Z. Galazka, T. Schulz, T. Remmele, T. Markurt, H. von Wenckstern, M. Grundmann, O. Bierwagen, P. Vogt, and M. Albrecht, Appl. Phys. Express 8, 011101 (2014).
- <sup>31</sup>G. Wagner, M. Baldini, D. Gogova, M. Schmidbauer, R. Schewski, M. Albrecht, Z. Galazka, D. Klimm, and R. Fornari, Phys. Status Solidi A 211, 27 (2014).
- <sup>32</sup>N. Moser, J. McCandless, A. Crespo, K. Leedy, A. Green, A. Neal, S. Mou, E. Ahmadi, J. Speck, K. Chabak, N. Peixoto, and G. Jessen, IEEE Electron Device Lett. 38, 775 (2017).
- <sup>33</sup> E. Ahmadi, O. S. Koksaldi, S. W. Kaun, Y. Oshima, D. B. Short, U. K. Mishra, and J. S. Speck, Appl. Phys. Express 10, 041102 (2017).
- <sup>34</sup>Y. Oshima, E. Ahmadi, S. Kaun, F. Wu, and J. S. Speck, Semicond. Sci. Technol. 33, 015013 (2017).
- <sup>35</sup> Z. Feng, A. F. M. Anhar Uddin Bhuiyan, M. R. Karim, and H. Zhao, Appl. Phys. Lett. 114, 250601 (2019).
- <sup>36</sup>A. Mauze, Y. Zhang, T. Itoh, F. Wu, and J. S. Speck, APL Mater. **8**, 021104 (2020)

- <sup>37</sup>G. Seryogin, F. Alema, N. Valente, H. Fu, E. Steinbrunner, A. T. Neal, S. Mou, A. Fine, and A. Osinsky, Appl. Phys. Lett. 117, 262101 (2020).
- <sup>38</sup>O. Kordina, C. Hallin, A. Ellison, A. S. Bakin, I. G. Ivanov, A. Henry, R. Yakimova, M. Touminen, A. Vehanen, and E. Janzén, Appl. Phys. Lett. 69, 1456 (1996).
- <sup>39</sup>O. Kordina, C. Hallin, A. Henry, J. P. Bergman, I. Ivanov, A. Ellison, N. T. Son, and E. Janzén, Phys. Status Solidi B 202, 321 (1997).
- <sup>40</sup> A. Kakanakova-Georgieva, R. R. Ciechonski, U. Forsberg, A. Lundskog, and E. Janzén, Cryst. Growth Des. 9, 880 (2009).
- <sup>41</sup> J.-T. Chen, I. Persson, D. Nilsson, C.-W. Hsu, J. Palisaitis, U. Forsberg, P. O. Å. Persson, and E. Janzén, Appl. Phys. Lett. 106, 251601 (2015).
- <sup>42</sup> J.-T. Chen, J. W. Pomeroy, N. Rorsman, C. Xia, C. Virojanadara, U. Forsberg, M. Kuball, and E. Janzén, J. Cryst. Growth 428, 54 (2015).
- <sup>43</sup> J.-T. Chen, J. Bergsten, J. Lu, E. Janzén, M. Thorsell, L. Hultman, N. Rorsman, and O. Kordina, Appl. Phys. Lett. 113, 041605 (2018).
- <sup>44</sup>J. Lu, J.-T. Chen, M. Dahlqvist, R. Kabouche, F. Medjdoub, J. Rosen, O. Kordina, and L. Hultman, Appl. Phys. Lett. **115**, 221601 (2019).
- <sup>45</sup> N. T. Son, C. P. Anderson, A. Bourassa, K. C. Miao, C. Babin, M. Widmann, M. Niethammer, J. Ul Hassan, N. Morioka, I. G. Ivanov, F. Kaiser, J. Wrachtrup, and D. D. Awschalom, Appl. Phys. Lett. 116, 190501 (2020).
- <sup>46</sup>H. Pedersen, S. Leone, A. Henry, F. C. Beyer, V. Darakchieva, and E. Janzén, J. Cryst. Growth **307**, 334 (2007).
- <sup>47</sup> H. Pedersen, S. Leone, A. Henry, V. Darakchieva, P. Carlsson, A. Gällström, and E. Janzén, Phys. Status Solidi RRL 2, 188 (2008).
- <sup>48</sup> K. J. Hüttinger, Chem. Vap. Deposition **4**, 151 (1998).
- <sup>49</sup>C is abundant in MOCVD process as a result of the metalorganic precursor cracking.
- <sup>50</sup>J. L. Lyons, D. Steiauf, A. Janotti, and C. G. Van de Walle, Phys. Rev. Appl. 2, 064005 (2014).
- <sup>51</sup> S. Mu, M. Wang, J. B. Varley, J. L. Lyons, D. Wickramaratne, and C. G. Van de Walle, Phys. Rev. B **105**, 155201 (2022).
- <sup>52</sup> A. Papamichail, A. Kakanakova, E. O. Sveinbjörnsson, A. R. Persson, B. Hult, N. Rorsman, V. Stanishev, S. P. Le, P. O. Persson, M. Nawaz, J. Chen, P. Paskov, and V. Darakchieva, J. Appl. Phys. 131, 185704 (2022).
- <sup>53</sup> L. Jones, H. Yang, T. J. Pennycook, M. S. Marshall, S. Van Aert, N. D. Browning, M. R. Castell, and P. D. Nellist, Adv. Struct. Chem. Imaging 1, 8 (2015).
- <sup>54</sup>Joint Committee on Powder Diffraction Standards (JCPDS), PDF no. 43043-1012 and 041-1103.
- <sup>55</sup>S. Rafique, L. Han, A. T. Neal, S. Mou, M. J. Tadjer, R. H. French, and H. Zhao, Appl. Phys. Lett. **109**, 132103 (2016).
- <sup>56</sup>R. Korlacki, J. Knudtson, M. Stokey, M. Hilfiker, V. Darakchieva, and M. Schubert, Appl. Phys. Lett. **120**, 042103 (2022).